Rapid hydrolysis of NO2 at high ionic strengths of deliquesced aerosol particles

Masao Gen

mgen@tohoku.ac.jp

Tohoku University

Haotian Zheng

Tsinghua University

Yele Sun

Institute of Atmospheric Physics, Chinese Academy of Sciences

Wanyun Xu

Chinese Academy of Meteorological Sciences

Nan Ma

Jinan University

Hang Su

Max Planck Institute for Chemistry https://orcid.org/0000-0003-4889-1669

Yafang Cheng

Max Planck Institute for Chemistry https://orcid.org/0000-0003-4912-9879

Shuxiao Wang

Tsinghua University

Jia Xing

Environmental Protection Agency

Shuping Zhang

Tsinghua University

Likun Xue

Shandong University

Chaoyang Xue

LPC2E-CNRS https://orcid.org/0000-0001-6673-7716

Yujing Mu

Research Center for Eco-Environmental Sciences, Chinese Academy of Sciences.
https://orcid.org/0000-0002-7048-2856

Xiao Tian

Nankai University

Atsushi Matsuki

Kanazawa University

Shaojie Song
Nankai University https://orcid.org/0000-0001-6395-7422

Article

Keywords:

Posted Date: December 6th, 2022

DOI: https://doi.org/10.21203/rs.3.rs-2257102/v1

Additional Declarations: There is **NO** Competing Interest.

Version of Record: A version of this preprint was published at Environmental Science & Technology on April 25th, 2024. See the published version at https://doi.org/10.1021/acs.est.3c08810.

Abstract

Nitrogen dioxide (NO_2) hydrolysis in deliquesced aerosol particles forms nitrous acid and nitrate and thus impacts air quality, climate, and nitrogen cycle. Traditionally, it is considered to proceed far too slowly in the atmosphere. However, the significance of this process is highly uncertain because kinetic studies have only been made in dilute aqueous solutions, and not under high ionic strength conditions of the aerosol particles. Here, we use laboratory experiments, air quality models, and field measurements to examine the effect of ionic strength on the reaction kinetics of NO_2 hydrolysis. We find that high ionic strengths (I) enhance the reaction rate constants (k_I) by more than two orders of magnitude compared to that at infinite dilution ($k_{I=0}$), yielding $\log_{10}(k_I/k_{I=0}) = 0.058I$. A state-of-the-art air quality model shows that the enhanced NO_2 hydrolysis reduces the negative bias in the simulated concentrations of nitrous acid by 27% on average when compared to field observations over the North China Plain. Rapid NO_2 hydrolysis also enhances the levels of nitrous acid in other polluted regions such as North India and further promotes atmospheric oxidation capacity. This study highlights the need to evaluate various reaction kinetics of atmospheric aerosols with high ionic strengths.

Main

Nitrogen dioxide (NO_2) is one of the most important reactive nitrogen species in the atmosphere and is emitted from combustion processes and atmospheric oxidation of nitric oxide [1]. In addition to its critical role in tropospheric photochemistry, NO_2 is involved in the multiphase or heterogeneous chemical reactions within cloud droplets and aerosol particles, affecting climate, air quality, human health, and ecosystems [2]. NO_2 hydrolysis in aqueous solution (R1) has long been known to produce nitrate (NO_3^-) and nitrite (NO_2^-) ions [3–8]. Nitrite undergoes the reversible acid-base reaction (R2). The produced nitrous acid is partitioned between the gas phase (designated as HONO) and aqueous phase (HNO_2) [9].

$$2NO_2(aq) + H_2O \rightarrow NO_2^- + NO_3^- + 2H^+ \quad \text{(R1)}$$

$$NO_2^- + H^+ \leftrightarrow HNO_2(aq) \leftrightarrow HONO(g) \quad \text{(R2)}$$

Nitrate is an increasingly important component in atmospheric aerosol particles with the trend of dominating over sulfate in places such as the North China Plain and the eastern United States [10,11]. HONO is a critical product as a primary source of hydroxyl radical (OH), the atmospheric “detergent” [12,13].

Traditionally, the reaction pathway R1 is considered to proceed far too slowly under ambient conditions. Its second-order reaction rate constant is reported to be 10^7–10^8 M^{-1} s^{-1} in pure water or dilute solution [3,4]. The uptake coefficient of NO_2 on pure water has been measured as small as 10^{-7} [3]. Hence, the reaction R1 is thought to contribute a negligible amount to reactive nitrogen cycle in the atmosphere. However, it is highly uncertain whether the reaction kinetics obtained from dilute solutions with low ionic

strengths are applicable to atmospheric aerosol particles which are often with much higher ionic strengths [14,15]. Ionic strength can greatly affect reaction kinetics occurring within deliquesced aerosol particles through its integrated effects on the activity coefficients of reactants and products [16,17]. In deliquesced aerosol particles, it is several orders of magnitude higher than that in cloud droplets (dilute conditions) and thermodynamic model calculations predict I values up to ~ 40 mol kg^{-1} [14]. To the best of our knowledge, reaction kinetics of NO_2 hydrolysis have not been measured under high ionic strength conditions, hampering our understanding of the significance of NO_2 hydrolysis in deliquesced aerosol particles.

In this study, we investigate the effect of ionic strength on the reaction kinetics of NO_2 hydrolysis in deliquesced aerosol particles. The experiments of NO_2 uptake by deliquesced particles were performed using a custom-made aerosol flow cell coupled with Raman spectroscope [18]; see the Methods for details on the uptake experiments, particle types to study, and data analysis. Seven types of particles were studied at various relative humidities (RHs) to achieve a wide range of I from 0.1 up to 44 mol kg^{-1}: 1) sodium chloride (NaCl); 2) ammonium chloride (NH_4Cl); 3) sodium sulfate (Na_2SO_4); 4) ammonium sulfate ($(NH_4)_2SO_4$); 5) ammonium bisulfate (NH_4HSO_4)/$(NH_4)_2SO_4$; 6) oxalic acid; and 7) malonic acid. Furthermore, we use a state-of-the-art chemical transport model, the Weather Research and Forecasting—Community Multiscale Air Quality (WRF-CMAQ) and incorporate in this model the enhancement effect of R1 due to the ionic strength of aerosols. The modeling results are then compared with field observations over the North China Plain to quantitatively examine its contribution in rectifying the model-observation gaps for nitrogen-containing species (NO_2, HONO, and particulate nitrate). Last, we evaluate the potential effect of this chemical mechanism on atmospheric oxidation capacity.

Ionic Strength Effect On Reaction Rate Constants

Our laboratory experiments show that nitrate formation rates are sensitive to gaseous NO_2 concentrations, and no nitrate is formed in the absence of NO_2 (Supplementary Fig. 1). The results ascertain that nitrate formation is driven by the heterogeneous hydrolysis reaction of NO_2 in aerosol particles. Figure 1A presents nitrate formation rates as a function of I for all particle types. All the experimental results are summarized in Supplementary Table 1. Nitrate formation rates are found to increase with decreasing RH (Supplementary Fig. 2) or increasing I values. Overall, we find that ionic strength has a positive influence on the reaction rates of R1. Notably, at high ionic strengths (I > 40 mol kg^{-1}), the formation rates become two orders of magnitude higher than those at low ionic strength (I < 1 mol kg^{-1}). Although the ionic strength influences the physical solubility or the Henry's law constant of gases in liquid water [19], NO_2 has a weak salting-out effect [20], and the high I does not enhance the solubility of NO_2 into liquid water. Hence, the observed increase of nitrate formation rates at high I are attributed to the enhanced reaction rate constants of R1.

Figure 1B summarizes the logarithm of the measured reaction rate constants at a given I, k_I, normalized by that at infinite dilution (i.e., $k_{I=0}$ = 10^8 mol^{-1} kg s^{-1}) as a function of I for all particle types examined. In non-ideal solutions, a reaction rate is proportional to reactant activities in place of the concentrations. The reactant activity is the product of its concentration and activity coefficient [21]. The activity coefficient is related to the ionic strength I [22], and hence a reaction rate is strongly affected by I (see details in Text S1 in Supplementary Information). For neutral species, its activity coefficient may be expressed as 10^{bI} according to the Debye and McAulay approach [23], where b is the kinetic salting coefficient [16]. Therefore, this ionic strength effect on reaction rate constants can be quantified as [16,24]:

$$\log_{10}(k_I) = \log_{10}(k_{I=0}) + bI \quad (1)$$

Equation (1) predicts that the logarithm of the ratio between k_I and $k_{I=0}$, $\log_{10}(k_I/k_{I=0})$, reaches zero as I decreases down to dilute conditions. Indeed, $\log_{10}(k_I/k_{I=0})$ has a strong linear dependence on I (Fig. 1B). Based on the Debye and McAulay framework, the positive dependence on I is attributable to an increase in the activity coefficient of reactant (i.e., NO_2) and/or the stabilization of the activated complex that is approximated by the bI term [16]. When I is less than 1 mol kg^{-1} (e.g., oxalic acid), k_I measured is 1.2 × 10^8 mol^{-1} kg s^{-1}, which is consistent with the rate constant obtained in dilute solutions [3]. Supplementary Table 2 shows that the rate constants determined in this study at high ionic strengths are several orders of magnitude higher than those in the literature under dilute conditions. These results highlight that the high ionic strengths of deliquesced aerosol particles significantly enhance NO_2 hydrolysis.

In contrast, k_I does not appear to be particularly sensitive to pH (Fig. 1B and Supplementary Fig. 3) and the chemical composition of the particles. For instance, Na_2SO_4 and NH_4HSO_4/$(NH_4)_2SO_4$ particles at 80% RH show comparable I and k_I values of 14.8 mol kg^{-1} and 1.8 × 10^9 mol^{-1} kg s^{-1}, and 15.3 mol kg^{-1} and 2.3 × 10^9 mol^{-1} kg s^{-1}, respectively, whereas they have different initial pH values of 5.6 and 0.9. Several studies report the effect of anions on NO_2 accommodation at air-aqueous interfaces. The presence of Cl^- in aqueous microdroplets significantly promotes the accommodation of gaseous NO_2 by Cl^- as Cl-NO_2^- at air-aqueous interfaces, followed by the reaction of Cl-NO_2^- with another NO_2 [25]. Carboxylic acids also catalyze the reaction of R1 at the air-particle interface. Colussi et al. [25] found an increased production of nitrate during the reaction by around 3 times as malonic acid concentrations increased from 0.01 to 0.1 mmol kg^{-1}. However, further increase in the acid concentration did not promote nitrate production. This suggests that the anion catalysis effect may be limited to the low ionic strength conditions (i.e., I < < 1 mol kg^{-1}). Our results (Fig. 1B) also show that the rate constant of R1 in malonic acid particles is about 4 times higher than in dilute solutions despite its low ionic strength of 0.1 mol kg^{-1}. Hence, the estimated rate constants may reflect the overall effects of ionic strength and catalysis by anions, particularly at low ionic strengths. Nonetheless, the ionic strength effect enhances the R1 reaction much more than the catalysis effect at high ionic strengths. We conclude that the ionic

strength effect can be a more important factor affecting the reaction kinetics at high ionic strengths of deliquesced aerosol particles. Thus, we have decided to simplify the parameterization of the kinetics using the ionic strength alone for model implementation. A linear fit (R^2 = 0.83, p < 0.05) to all the data points in Fig. 1B yields b = 0.058 in Eq. (1), which primarily represents the ionic strength effect. This quantitative relationship is used in the model analysis described in the next section.

Model Analysis And Evaluation With Field Observations

To examine the significance of the ionic strength effect on heterogeneous NO_2 hydrolysis, we incorporate the effect of ionic strength into the WRF-CMAQ air quality modeling system and evaluate the model performance against field observations over the North China Plain (NCP). This region is chosen because intensive anthropogenic emissions lead to high NO_2 levels and aerosol loadings, which are expected to facilitate the heterogeneous hydrolysis of NO_2 [26,27]. The field observations were taken during 2015–2018 at five stations (Supplementary Fig. 4) and the sampling periods have been summarized in Supplementary Table 3 [28–32]. For all the stations, we compare the observed and modeled concentrations of NO_2 and HONO (particulate nitrate data were not available at some stations). Two WRF-CMAQ modeling scenarios, namely, Base and IS_Enh, are analyzed in this section. The Base scenario generally follows the default WRF-CMAQ settings, whereas the IS_Enh scenario differs in considering the enhancement effect of ionic strength on the reaction rates of heterogeneous NO_2 hydrolysis using the exponential relationship obtained from our laboratory experiments (see the Methods).

The model–observation comparisons of HONO concentrations are shown in Fig. 2 and Supplementary Table 4. The observed HONO concentrations exhibit both seasonal and spatial variations. The highest mean value 2.8 parts per billion (ppb) was obtained during the wintertime at Gucheng, while the lowest mean (0.2 ppb) was found during the summertime at Dongying, Shandong Province. The linear regression analysis suggests that the Base and IS_Enh modeling scenarios can explain 69% and 75% of the variance in HONO observations, respectively. The Base scenario greatly underestimates the concentrations of HONO by more than a half, although it has considered various HONO sources including direct emissions from biomass burning and motor vehicles, homogeneous reaction of OH and nitric oxide (NO), and heterogeneous reactions of NO_2 on ground surfaces and deliquesced aerosols (without ionic strength effect). The IS_Enh scenario reduces the low bias by 27% on average, demonstrating the significant enhancement effect of ionic strength on heterogeneous NO_2 hydrolysis. Both scenarios predict NO_2 concentrations which agree well with the field observations over the NCP, and heterogeneous NO_2 hydrolysis has a very minor effect on the levels of NO_2 (Supplementary Fig. 5). The stoichiometric factor of HONO/NO_2 is 1:2 in R1, while the level of HONO is commonly 1–2 orders of magnitude lower than that of NO_2; therefore, this reaction pathway is more important to HONO.

A more detailed comparison is made for the McFAN campaign (Multiphase chemistry experiment in Fogs and Aerosols in the North China Plain) conducted at Gucheng, Hebei Province during winter 2018

since all the relevant meteorological variables and chemical species are available [28]. Time series of the observed and simulated concentrations of NO_2, HONO, and particulate nitrate during the McFAN field campaign are shown in Supplementary Fig. 6 and the model performance is summarized in Table 1. Generally, the simulated NO_2 concentrations agree well with the McFAN observation in the Base scenario with a normalized mean bias (NMB) of 8%. However, HONO concentrations are significantly underestimated in the Base scenario with a NMB of − 49% and this bias is evident during both daytime and nighttime. Similarly, nitrate concentrations are underestimated with a NMB of − 34%. In the IS_Enh scenario, the ionic strength enhancement effect significantly improves the simulated NO_2, HONO, and nitrate concentrations and reduces their NMB values (Table 1).

Table 1
Statistics of model performance during the McFAN campaign.

Species	Time	Observation	Base Scenario		IS_Enh Scenario	
		Conc.	**Conc.**	**NMB* (%)**	**Conc.**	**NMB (%)**
NO_2 (ppb)	Daytime	30.0	31.7	4.0	30.3	−0.6
	Nighttime	39.7	43.7	9.4	40.7	1.9
	Average	36.1	39.2	7.7	36.8	1.1
HONO (ppb)	Daytime	1.6	0.4	−74.7	0.6	−60.6
	Nighttime	3.5	1.9	−41.8	3.1	−8.9
	Average	2.8	1.3	−48.8	2.1	−19.9
Nitrate ($\mu g\ m^{-3}$)	Daytime	14.6	7.7	−47.1	10.7	−26.5
	Nighttime	12.8	9.3	−26.5	14.7	16.5
	Average	13.4	8.7	−34.4	13.2	0.1

*NMB refers to normalized mean bias.

Figure 3 shows the diurnal patterns of two meteorological parameters (RH and downward shortwave radiation) and three nitrogen-containing chemical species in the McFAN campaign. The simulated nighttime HONO in the IS_Enh scenario is close to the observations with a NMB of − 9%. However, the simulated HONO during the daytime only shows a slight improvement (from − 75% to − 61%). The diurnal difference can be attributed to two factors. First, elevated shortwave radiation during the daytime enhances the photolysis of HONO, making the extra HONO formed in this pathway (R1) photolyze quickly, which can be observed from the integrated reaction rate analysis (IRR) results in Supplementary Fig. 7. Second, the relatively low RH during the daytime (Fig. 3A) may result in a hygroscopic growth factor (HGF) smaller than the criterion for the aerosol solid–liquid phase state transition, thus hindering the

enhancement effect (Supplementary Fig. 8). Overall, the enhanced NO_2 hydrolysis rate due to the ionic strength effect leads to significantly better model performance of HONO and nitrate, particularly during the nighttime, while it hardly affects the satisfying NO_2 results.

Impact On Nitrogen-containing Species And Atmospheric Oxidation Capacity

The WRF-CMAQ simulated difference between the IS_Enh and Base scenarios is used to examine the influence of rapid NO_2 hydrolysis on nitrogen-containing species and atmospheric oxidation capacity. Figure 4 shows the modeled surface concentrations of HONO and nitrate over East Asia during winter. The most significant areas are the NCP (marked in square in Fig. 4) and North India, as well as parts of Northeast China and Republic of Korea. It is shown that surface concentrations of HONO and nitrate over the NCP and North India increase by 71% and 10%, and 96% and 9%, respectively, in the IS_Enh model scenario when compared to the Base. Field measurements of HONO are still rare in India, and a very recent study[33] observed high levels of HONO of about 3 ppb during winter in Delhi, similar to its value found in the NCP. During summer, the difference between the IS_Enh and Base scenarios is minor (Supplementary Fig. 9). Two factors are considered to contribute to this seasonal variation. First, frequent temperature inversion events in winter result in high levels of NO_x, aerosol, and water vapor being accumulated in the shallow planetary boundary layer, providing abundant precursor and reaction space for heterogeneous NO_2 hydrolysis [29,34]. Second, the stronger and longer solar radiation during summer enhances the photolysis of HONO and thus hampers its accumulation.

The formation of HONO can further enhance the atmospheric oxidation capacity through its photolysis and the subsequent free radical reactions (Supplementary Fig. 10). Over the NCP during winter, the modeled OH and O_3 concentrations in the IS_Enh scenario are 19% and 6% higher, respectively, compared to those in the Base scenario. Nevertheless, the ionic strength effect of heterogeneous NO_2 hydrolysis has little influence during summer (< 0.1% increase in OH and O_3).

Discussion

The present study has demonstrated the significant enhancement of NO_2 hydrolysis rate constants under high ionic strengths. There are caveats in this study. First, whereas the enhancement effect significantly improves the model prediction of nighttime HONO, there remains a big gap between the modeled and observed HONO during the daytime (Table 1). This could be attributed to several factors. (*i*) our experiments were carried out under dark conditions and thus unable to analyze the synergistic effect of ionic strength and solar radiation on heterogeneous NO_2 hydrolysis. There has been evidence indicating the enhancement of reaction rates by solar radiation [35,36]. (*ii*) Zhou et al. [37] have suggested that nitric acid and nitrate may undergo rapid photolysis on environmental surfaces, leading to HONO production during the daytime. Photolysis of particulate nitrate is also a potentially important source for

HONO [38,39], but its importance heavily depends on the highly uncertain rates of nitrate photolysis [40,41]. (*iii*) the reaction of NO_2 with SO_2 in aerosol water has attracted great attention because it produces HONO as well as sulfate [42,43]. Future laboratory and modeling studies are required to clarify the contributions of these chemical mechanisms to ambient HONO levels during the daytime.

Second, our laboratory experiments were conducted at room temperature while the ambient temperature varies with time and location. Previous studies [1,44] have suggested that both the rate constant of R1 and the solubility of NO_2 in dilute aqueous solutions change with temperature, and that these two effects offset each other to some extent. An additional WRF-CMAQ modeling scenario, IS_Enh_T, was performed to evaluate the temperature effects. As shown in Supplementary Table 4, the IS_Enh_T scenario results in slightly higher HONO concentrations in winter (~ 10%) while it hardly affects the simulations in summer (< 3%).

Last, the reaction kinetics obtained in dilute aqueous solutions with low ionic strengths have been widely applied to the high ionic strength conditions in atmospheric aerosol particles, but their applicability is highly uncertain. Reaction rate enhancements at the high ionic strengths are not be limited to the current reaction system (i.e., NO_2 hydrolysis) but arise for other reaction systems [17,45]. On the other hand, reduction in reaction rates due to high ionic strengths may also be relevant to certain systems such as the reaction of dissolved SO_2 with transition metal ions [46,47]. Our study underscores the need to evaluate various reaction kinetics of atmospheric aerosols with high ionic strengths.

Methods

Materials

We prepared aqueous stock solutions of NaCl (99%, Wako Chemicals), NH_4Cl (98.5%, Wako Chemicals), Na_2SO_4 (99%, Wako Chemicals), $(NH_4)_2SO_4$ (99.5%, Wako Chemicals), NH_4HSO_4 (98%, Wako Chemicals), oxalic acid (98%, Wako Chemicals), and malonic acid (99%, Sigma-Aldrich) by dissolving the corresponding salt into ultrapure water. Seven types of particles were examined in this study. Aqueous droplets were atomized from the stock solutions using a piezoelectric microdroplet dispenser (MJ-ABP-01-60, Microfab) supplied with a voltage pulse from an amplifier (PDm200, PiezoDrive). The droplets were deposited on a hydrophobic substrate (model 5793, YSI Inc.) to maintain the spherical shape. The volume-weighted size of the droplets was on average 40 μm.

No Uptake Experiments

Faced with the necessity for good control of ionic strengths of aerosol particles, we performed NO_2 uptake experiments with particles using a custom-made aerosol flow cell that is an open system under continuous air flow [18,48]. The cell has a quartz window for Raman analysis. Various chemical compositions of the particles and RH values were used to realize a wide range of ionic strength from 0.1

up to 44 mol kg^{-1}. We used organic acid particles to create low ionic strength situations (< 1 mol kg^{-1}) given that organic anions are not present as main species at low particle pH. The Extended Aerosol Inorganics Model (E-AIM) [49,50] predicts the pH values of 0.14 and 0.9 at 80% RH, and the mole fractions of ionic species in the total organic acid are 6% and 1% for oxalic acid and malonic acid particles, respectively. RH values examined for oxalic acid and malonic acid particles were limited to 80% RH because the ionic strength of the particles does not dramatically change with RH. RH in the flow cell was controlled using a mixed flow of dry and wet gas streams of compressed air and measured with a RH sensor (HC2-C05, Rotronic). The air from the compressor was dried by a heatless dryer and filtered using a high-efficiency particulate air filter (Supplementary Fig. 11). Standard NO_2 gas (Taiyo Nippon Sanso) was introduced into the cell to initiate the reaction, and the NO_2 concentration in the cell was 10 ppm and maintained throughout the experiments. All experiments were conducted at ~ 20°C. Note that the NO_2 concentration used in this study (10 ppm) was higher than that in the atmosphere, although the participation of the dimer (N_2O_4) in the reaction [7] was insignificant [25]. The concentration difference might result in different reaction kinetics. However, we measured the reaction rate constant that is generally unaffected by reactant concentration, or gas concentration in heterogeneous reactions. When heterogeneous reactions of NO_2 mainly take place at the surface, their rate constants increase with decreasing gas concentration due to the Langmuir – Hinshelwood behavior [51]. If this is the case, our results suggest that the reaction rate constants of R1 would be further enhanced at atmospherically relevant NO_2 concentrations. This will reinforce the importance of the ionic strength enhancement effect, and our estimates of the rate constants may be conservative.

Raman Analysis

Particles deposited on a hydrophobic substrate were in-situ analyzed using micro-Raman spectroscope (Nanofinder HE, Tokyo Instruments). Raman spectra were obtained at 100–4200 cm^{-1} with a 13 mW 532 nm laser. A 20× objective lens (numerical aperture of 0.45, LUCPLFLN20X, Olympus) was used to guide the laser onto the particle. We calibrated the peak position in the spectra against the known Raman signal of a pure silicon standard at 520 cm^{-1}. Nitrate formed in the particle was quantified from Raman peak area ratios of nitrate (1050 cm^{-1}) to water (~ 3400 cm^{-1}) using the calibration curve established between the peak area ratios and standard nitrate aqueous solutions of known concentration (Supplementary Fig. 12). Time-series Raman spectra obtained showed nitrate formation as a reaction product and its intensity increases with reaction time (Supplementary Fig. 13).

Determination Of Rate Constant

Reaction rate constant of R1, k_I, at a given ionic strength, I, was determined from the formation rate of nitrate, $d[NO_3^-]/dt$ [3]:

$$\frac{d[NO_3^-]}{dt} = k_I[NO_2(aq)]^2 \quad \text{(M1)}$$

where $[NO_2(aq)]$ is the concentration of dissolved NO_2 calculated by the product of the Henry's law constant of and the gas concentration of NO_2. The ionic strength of the particles was estimated using the E-AIM model with the relative concentrations of the solutes in the particles and meteorological variables (RH and temperature) as inputs. The rate constant is reported to be 10^8 M^{-1} s^{-1} at infinite dilution [3]. Hence, the molality-based rate constant is approximated to 10^8 mol^{-1} kg s^{-1} (i.e., $k_{I=0}$ = 10^8 mol^{-1} kg s^{-1}) assuming the density is the same as water density (1 kg L^{-1}), and is used to obtain $\log_{10}(k_I/k_{I=0})$ (Fig. 1B). Note that the rate constants in the earlier work were reported in the unit of M^{-1} s^{-1}, whereas we employ the molality-based rate constants (i.e., mol^{-1} kg s^{-1}). For dilute solutions, these two units are essentially the same. For solutions with high ionic strengths (i.e., aerosol liquid water), the molality-based values are larger than the molarity-based ones at a given ionic strength as the solution density becomes larger than the density of water. Nonetheless, the difference between the solution and water densities should be much smaller than the observed enhancement of the rate constants at high ionic strengths.

The reaction R1 also produces nitrite, which was not detected in our Raman measurements. The absence of nitrite is attributed to the partitioning into the gas phase as HONO given low Henry's law constant (49 M atm^{-1}) [52]. Bambauer et al. [53] also found a substantial low ratio of nitrite to nitrate from the reaction R1 on acidified microdroplets (pH < 5), whereas approximately equal nitrite and nitrate concentrations were observed at pH > 5. In this study, initial pH of the particles predicted by the E-AIM model was below around 5 (Supplementary Table 1) and the pH values during reaction will be likely lower than the initial pH because hydrogen ion is produced in R1. Hence, this study focuses on nitrate production to determine the reaction rate constant.

WRF-CMAQ Model Development And Configuration

The modeling domain is shown in Supplementary Fig. 4 with a 27 km × 27 km horizontal resolution and 14 vertical layers from ground surface to 100 hPa. The WRF model (version 3.9.1) was used to simulate the meteorological fields and its physical options were configurated the same as those in Zheng et al. [54]. The meteorological observational data (including temperature, RH, and wind velocity) at more than 2000 stations collected by the Chinese Meteorological Administration were assimilated in the WRF simulation for better model performance (http://data.cma.cn/en/, last access: 1 November 2022). In the CMAQ model (version 5.3.3), the Carbon Bond 6 (CB6) and AERO7 mechanisms were selected for gas phase and aerosol chemistry simulations, respectively. The modeling period covered all the periods shown in Supplementary Table 3 and the January and July of 2018. The monthly average concentrations in the January and July of 2018 were used to represent those in winter and summer seasons, respectively. A 5-

day spin-up period was applied. The NCEP FNL (Final) operational global reanalysis data (https://rda.ucar.edu/datasets/ds083.2/, last access: 1 November 2022) provided initial and boundary conditions for the WRF model and the default (clean) boundary conditions were selected for the CMAQ model.

The anthropogenic emissions over China for the years 2015 to 2018 were obtained from the Air Benefit and Cost and Attainment Assessment System (ABaCAS) emission inventory [55]. The emission inventory of IIASA-ECLIPSE (V5) was applied over the rest of the modeling domain [56]. The emitted species include trace gases (SO_2, NO_x, NH_3, and volatile organic compounds) and primary PM (dust, black carbon, and organic carbon). Moreover, HONO emissions from motor vehicles were considered based on an empirical ratio between HONO and NO_x (HONO/NO_x = 8.0 mmol mol^{-1}) [29]. In addition, we included HONO emissions from biomass burning based on the ratio between HONO and CO, whose value (HONO/CO = 3.4 mmol mol^{-1}) was estimated using the geometric mean of the reported uncertainty range [57]. The soil emission of HONO was not included since previous WRF-CMAQ modeling studies suggested that its impact was very low [29].

Secondary formation of HONO in the standard CMAQ model involves both homogeneous and heterogenous pathways. Three gas-phase chemical reactions (M2–M4) are included in CB6 and their kinetics can be found in Zhang et al. [29]:

$$NO + OH \rightarrow HONO \quad \text{(M2)}$$

$$NO + NO_2 + H_2O \rightarrow 2HONO \quad \text{(M3)}$$

$$\text{nitro-creso} \xrightarrow{h\nu} HONO + HO_2 + HCHO + OPEN \quad \text{(M4)}$$

where OPEN refers to aromatic ring open product.

Two heterogeneous processes, hydrolyses of NO_2 on ground surfaces and deliquesced aerosol particles, are considered in the standard CMAQ model. Ground surface areas are provided by leaves (estimated using leaf area index) as well as buildings and other structures in urban environments [58]. The rate constant of heterogeneous NO_2 hydrolysis on aerosol surfaces, k_{het}, is described as:

$$k_{het} = \frac{1}{4} \times \frac{S}{V} \times v \times \left[\frac{1}{\alpha} + \frac{1}{\gamma}\right]^{-1} \quad \text{(M5)}$$

where S/V ($m^2\ m^{-3}$ air) is the aerosol surface area per unit volume of air, v ($m\ s^{-1}$) is the mean molecular speed of NO_2, a is the mass accommodation coefficient of NO_2 [44], and g is the heterogeneous uptake coefficient of NO_2. A hygroscopic growth factor (HGF) of 1.15 is taken as the criterion for determining the aerosol liquid state [59]. In the CMAQ model, HGF was calculated as follows:

$$\mathrm{HGF}=\sqrt[3]{\left(\sum_i {m_i}/{\rho_i}+{m_{\mathrm{water}}}/{\rho_{\mathrm{water}}}\right)\Big/\sum_i {m_i}/{\rho_i}} \quad \text{(M6)}$$

where m_i and ρ_i represent the mass concentration (mg m^{-3}) and density (g cm^{-3}) of the i^{th} soluble ion, respectively. The densities of SNA (SO_4^{2-}, NO_3^-, NH_4^+), Cl^-, dust, and water were chosen as 1.75, 1.52, 2.7, and 1.0 g cm^{-3}, respectively [60].

Three WRF-CMAQ modeling scenarios, Base, IS_Enh, and IS_Enh_T, are conducted in this study. The integrated reaction rate (IRR) analysis was applied in the CMAQ model to quantify the contribution of each chemical source and loss pathway for HONO. In the Base scenario, the heterogeneous NO_2 uptake coefficient g was set to be 1.4×10^{-6}, the geometric mean of its reported uncertainty range [35]. In the IS_Enh scenario, in consideration of the ionic strength effect, g was multiplied by a factor of $10^{0.058I}$ when the aerosol particles are in a liquid phase, as suggested by our laboratory experiments. The IS_Enh_T scenario differs from the IS_Enh in considering the effect of temperature on heterogeneous uptake coefficient of NO_2. Note that the parameterization of temperature dependence under high ionic strength conditions has not been available yet and here we adopt the reported values for dilute conditions [1,44]. The differences between Base and IS_Enh scenarios denote the influence of the ionic strength while the differences between IS_Enh and IS_Enh_T scenarios represent the influence of temperature.

Field Observations

Measurement data of HONO and NO_2 concentrations were obtained from five surface stations in the North China Plain (Supplementary Fig. 4). The sampling time periods are summarized in Supplementary Table 3. Experimental details have been described in detail in the literature [28–32]. Specifically, the Multiphase chemistry experiment in Fogs and Aerosols in the North China Plain (McFAN) campaign was conducted during winter 2018 at the Gucheng site (39°09' N, 115°44' E) in Heibei province, China. This site is surrounded by agricultural fields and small residential towns and is considered to represent the pollution regime of the North China Plain [28]. The chemical compositions (organics, sulfate, nitrate, ammonium, and chloride) of nonrefractory submicron aerosol particles (PM_1) were measured using an Aerodyne ToF-ACSM (Time-of-Flight Aerosol Chemical Speciation Monitor). The concentrations of HONO were analyzed by a LOng Path Absorption Photometer (LOPAP). The meteorological parameters were provided by the collocated Ecological and Agricultural Meteorology Station of the Chinese Academy of Meteorological Sciences. The concentrations of NO_2 were obtained from a nearby national air quality monitoring station (38°52' N, 115°31' E). More details on the sampling site and ambient measurements have been described in the literature [28,61,62]. The measurement period of 16–30 November 2018 was used in our analysis when the necessary data are all available.

We evaluated the WRF-CMAQ model performance by comparing the simulation results with the observational data. The normalized mean bias (NMB) is used as the performance metric and is calculated as [63]:

$$\mathrm{NMB} = \frac{\sum \left(C_{\mathrm{m}} - C_{\mathrm{o}} \right)}{\sum C_{\mathrm{o}}} \qquad \text{(M7)}$$

where C_{m} and C_{o} refer to the modeled and observed concentrations, respectively.

Declarations

Acknowledgements

We thank Y. Sasaki and K. Suzuki for assistance with Raman experiments, and data analysis. This work was supported by the Japan Science and Technology Agency (JST) for Fusion Oriented Research for disruptive Science and Technology program (JPMJFR206V), the Japan Society for the Promotion of Science (JSPS) Grants-in-Aid for Early-Career Scientists (21K17876), National Natural Science Foundation of China (22188102, 42205109), and the Open Project of CMA-NKU Cooperative Laboratory for Atmospheric Environment-Health Research (CMANKU202201). S.W. thanks the support from Tencent Foundation through the XPLORER PRIZE. S.S. thanks the support by TianHe Qingsuo open research fund of TSYS in 2022 & NSCC-TJ.

Author contributions

M.G. and S.S. conceived the study. M.G. performed Raman experiments, analyzed data, constructed equipment, and wrote the manuscript. H.Z. and S.S. performed chemical transport modeling and wrote the manuscript. Y.S., W.X., N.M., H.S., Y.C., L.X., C.X., and Y.M. contributed to field observations. S.W., J.X., S.Z., and X.T. contributed to chemical transport modeling. A.M. contributed to laboratory experiments. All authors read and commented on the manuscript.

Competing interests

The authors declare no competing interests.

References

1. Seinfeld, J. H. & Pandis, S. N. *Atmospheric Chemistry and Physics: From Air Pollution to Climate Change*. *Atmospheric Chemistry and Physics* (Wiley, 2006).
2. Su, H., Cheng, Y. & Pöschl, U. New multiphase chemical processes influencing atmospheric aerosols, air quality, and climate in the anthropocene. Acc. Chem. Res. **53**, 2034–2043 (2020).

3. Lee, Y. N. & Schwartz, S. E. Reaction kinetics of nitrogen dioxide with liquid water at low partial pressure. J. Phys. Chem. **85**, 840–848 (1981).
4. Cheung, J. L. *et al.* Heterogeneous interactions of NO_2 with aqueous surfaces. J. Phys. Chem. A **104**, 2655–2662 (2000).
5. Park, J. Y. & Lee, Y. N. Solubility and decomposition kinetics of nitrous acid in aqueous solution. J. Phys. Chem. **92**, 6294–6302 (1988).
6. Cape, J. N., Storeton-West, R. L., Devine, S. F., Beatty, R. N. & Murdoch, A. The reaction of nitrogen dioxide at low concentrations with natural waters. Atmos. Environ. Part A. Gen. Top. **27**, 2613–2621 (1993).
7. Finlayson-Pitts, B. J., Wingen, L. M., Sumner, A. L., Syomin, D. & Ramazan, K. A. The heterogeneous hydrolysis of NO_2 in laboratory systems and in outdoor and indoor atmospheres: An integrated mechanism. Phys. Chem. Chem. Phys. **5**, 223–242 (2003).
8. Li, L., Hoffmann, M. R. & Colussi, A. J. Role of nitrogen dioxide in the production of sulfate during chinese haze-aerosol episodes. Environ. Sci. Technol. **52**, 2686–2693 (2018).
9. Su, H. *et al.* Soil nitrite as a source of atmospheric HONO and OH radicals. Science **333**, 1616–1618 (2011).
10. Fu, X. *et al.* Persistent heavy winter nitrate pollution driven by increased photochemical oxidants in northern China. Environ. Sci. Technol. **54**, 3881–3889 (2020).
11. Shah, V. *et al.* Chemical feedbacks weaken the wintertime response of particulate sulfate and nitrate to emissions reductions over the eastern United States. *Proc. Natl. Acad. Sci.* **115**, 8110–8115 (2018).
12. Lee, J. D. *et al.* Detailed budget analysis of HONO in central London reveals a missing daytime source. Atmos. Chem. Phys. **16**, 2747–2764 (2016).
13. Su, H. *et al.* Nitrous acid (HONO) and its daytime sources at a rural site during the 2004 PRIDE-PRD experiment in China. J. Geophys. Res. Atmos. **113**, D14312 (2008).
14. Cheng, Y. *et al.* Reactive nitrogen chemistry in aerosol water as a source of sulfate during haze events in China. Sci. Adv. **2**, e1601530 (2016).
15. Cheng, Y., Su, H., Koop, T., Mikhailov, E. & Pöschl, U. Size dependence of phase transitions in aerosol nanoparticles. Nat. Commun. **6**, 5923 (2015).
16. Herrmann, H. Kinetics of aqueous phase reactions relevant for atmospheric chemistry. Chem. Rev. **103**, 4691–4716 (2003).
17. Liu, T., Clegg, S. L. & Abbatt, J. P. D. Fast oxidation of sulfur dioxide by hydrogen peroxide in deliquesced aerosol particles. *Proc. Natl. Acad. Sci. U. S. A.* **117**, 1354–1359 (2020).
18. Gen, M., Zhang, R., Huang, D. D., Li, Y. & Chan, C. K. Heterogeneous SO_2 oxidation in sulfate formation by photolysis of particulate nitrate. Environ. Sci. Technol. Lett. **6**, 86–91 (2019).
19. Kampf, C. J. *et al.* Effective Henry's law partitioning and the salting constant of glyoxal in aerosols containing sulfate. Environ. Sci. Technol. **47**, 4236–4244 (2013).

20. Squadrito, G. L. & Postlethwait, E. M. On the hydrophobicity of nitrogen dioxide: Could there be a “lens” effect for NO_2 reaction kinetics? Nitric Oxide **21**, 104–109 (2009).
21. Brönsted, J. N. Zur Theorie der chemischen Reaktionsgeschwindigkeit. Zeitschrift für Phys. Chemie **102U**, 169–207 (1922).
22. Long, F. A. & McDevit, W. F. Activity coefficients of nonelectrolyte solutes in aqueous salt solutions. Chem. Rev. **51**, 119–169 (1952).
23. Debye, P. & McAulay, J. Das elektrische Feld der Ionen und die Neutralsalzwirkung. Phys. Zeitschr **26**, 22–29 (1925).
24. Chen, Z. *et al.* Rapid sulfate formation via uncatalyzed autoxidation of sulfur dioxide in aerosol microdroplets. Environ. Sci. Technol. **56**, 7637–7646 (2022).
25. Colussi, A. J. *et al.* Tropospheric aerosol as a reactive intermediate. Faraday Discuss. **165**, 407–420 (2013).
26. Wei, J. *et al.* Ground-level NO_2 surveillance from space across China for high resolution using interpretable spatiotemporally weighted artificial intelligence. Environ. Sci. Technol. **56**, 9988–9998 (2022).
27. van Donkelaar, A. *et al.* Monthly global estimates of fine particulate matter and their uncertainty. Environ. Sci. Technol. **55**, 15287–15300 (2021).
28. Li, G. *et al.* Multiphase chemistry experiment in Fogs and Aerosols in the North China Plain (McFAN): integrated analysis and intensive winter campaign 2018. Faraday Discuss. **226**, 207–222 (2021).
29. Zhang, S. *et al.* Improving the representation of HONO chemistry in CMAQ and examining its impact on haze over China. Atmos. Chem. Phys. **21**, 15809–15826 (2021).
30. Gu, R. *et al.* Investigating the sources of atmospheric nitrous acid (HONO) in the megacity of Beijing, China. Sci. Total Environ. **812**, 152270 (2022).
31. Li, D. *et al.* Characteristics and sources of nitrous acid in an urban atmosphere of northern China: Results from 1-yr continuous observations. Atmos. Environ. **182**, 296–306 (2018).
32. Gu, R. *et al.* Atmospheric nitrous acid (HONO) at a rural coastal site in North China: Seasonal variations and effects of biomass burning. Atmos. Environ. **229**, 117429 (2020).
33. Acharja, P. *et al.* Enhanced secondary aerosol formation driven by excess ammonia during fog episodes in Delhi, India. Chemosphere **289**, 133155 (2022).
34. Xu, Q. *et al.* Nitrate dominates the chemical composition of $PM_{2.5}$ during haze event in Beijing, China. Sci. Total Environ. **689**, 1293–1303 (2019).
35. Liu, Y. *et al.* A Comprehensive model test of the HONO sources constrained to field measurements at rural North China Plain. Environ. Sci. Technol. **53**, 3517–3525 (2019).
36. Liu, J. *et al.* Physical and chemical characterization of urban grime: An impact on the NO_2 uptake coefficients and N-containing product compounds. Sci. Total Environ. **838**, 155973 (2022).
37. Ma, Q. *et al.* Comprehensive study about the photolysis of nitrates on mineral oxides. Environ. Sci. Technol. **55**, 8604–8612 (2021).

38. Gen, M., Liang, Z., Zhang, R., Go Mabato, B. R. & Chan, C. K. Particulate nitrate photolysis in the atmosphere. Environ. Sci. Atmos. **2**, 111–127 (2022).
39. Gen, M., Zhang, R., Huang, D. D., Li, Y. & Chan, C. K. Heterogeneous oxidation of SO_2 in sulfate production during nitrate photolysis at 300 nm: Effect of pH, relative humidity, irradiation intensity, and the presence of organic compounds. Environ. Sci. Technol. **53**, 8757–8766 (2019).
40. Romer, P. S. *et al.* Constraints on aerosol nitrate photolysis as a potential source of HONO and NOx. Environ. Sci. Technol. **52**, 13738–13746 (2018).
41. Shi, Q. *et al.* Laboratory investigation of renoxification from the photolysis of inorganic particulate nitrate. Environ. Sci. Technol. **55**, 854–861 (2021).
42. Sicard, P. *et al.* Amplified ozone pollution in cities during the COVID-19 lockdown. Sci. Total Environ. **735**, 139542 (2020).
43. Bloss, W. J. *et al.* Insights into air pollution chemistry and sulphate formation from nitrous acid (HONO) measurements during haze events in Beijing. Faraday Discuss. **226**, 223–238 (2021).
44. Ammann, M. *et al.* Evaluated kinetic and photochemical data for atmospheric chemistry: Volume VI – heterogeneous reactions with liquid substrates. Atmos. Chem. Phys. **13**, 8045–8228 (2013).
45. Chen, T. *et al.* Enhancement of aqueous sulfate formation by the coexistence of NO_2/NH_3 under high ionic strengths in aerosol water. Environ. Pollut. **252**, 236–244 (2019).
46. Wang, W. *et al.* Sulfate formation is dominated by manganese-catalyzed oxidation of SO_2 on aerosol surfaces during haze events. Nat. Commun. **12**, 1993 (2021).
47. Martin, L. R. & Hill, M. W. The iron catalyzed oxidation of sulfur: Reconciliation of the literature rates. Atmos. Environ. **21**, 1487–1490 (1967).
48. Gen, M., Huang, D. D. & Chan, C. K. Reactive uptake of glyoxal by ammonium-containing salt particles as a function of relative humidity. Environ. Sci. Technol. **52**, 6903–6911 (2018).
49. Clegg, S. L., Brimblecombe, P. & Wexler, A. S. Thermodynamic model of the system H^+-NH_4^+-SO_4^{2-}-NO_3^--H_2O at Tropospheric Temperatures. J. Phys. Chem. A **102**, 2137–2154 (1998).
50. Clegg, S. L., Brimblecombe, P. & Wexler, A. S. Thermodynamic model of the system H^+-NH_4^+-Na^+-SO_4^{2-}-NO_3^--Cl^--H_2O at 298.15 K. J. Phys. Chem. A **102**, 2155–2171 (1998).
51. Liu, J. *et al.* Light-enhanced heterogeneous conversion of NO_2 to HONO on solid films consisting of fluorene and fluorene/Na_2SO_4: An impact on urban and indoor atmosphere. Environ. Sci. Technol. **54**, 11079–11086 (2020).
52. Sander, R. Compilation of Henry's law constants (version 4.0) for water as solvent. Atmos. Chem. Phys. **15**, 4399–4981 (2015).
53. Bambauer, A., Brantner, B., Paige, M. & Novakov, T. Laboratory study of NO_2 reaction with dispersed and bulk liquid water. Atmos. Environ. **28**, 3225–3232 (1994).
54. Zheng, H. *et al.* Contribution of particulate nitrate photolysis to heterogeneous sulfate formation for winter haze in china. Environ. Sci. Technol. Lett. **7**, 632–638 (2020).

55. Zheng, H. *et al.* Transition in source contributions of $PM_{2.5}$ exposure and associated premature mortality in China during 2005–2015. Environ. Int. **132**, 105111 (2019).
56. Klimont, Z. *et al.* Global anthropogenic emissions of particulate matter including black carbon. Atmos. Chem. Phys. **17**, 8681–8723 (2017).
57. Zhang, J. *et al.* Impacts of six potential HONO sources on HOx budgets and SOA formation during a wintertime heavy haze period in the North China Plain. Sci. Total Environ. **681**, 110–123 (2019).
58. Sarwar, G. *et al.* A comparison of CMAQ HONO predictions with observations from the Northeast Oxidant and Particle Study. Atmos. Environ. **42**, 5760–5770 (2008).
59. Bateman, A. P., Bertram, A. K. & Martin, S. T. Hygroscopic influence on the semisolid-to-liquid transition of secondary organic materials. J. Phys. Chem. A **119**, 4386–4395 (2015).
60. Salcedo, D. *et al.* Characterization of ambient aerosols in Mexico City during the MCMA-2003 campaign with Aerosol Mass Spectrometry: results from the CENICA Supersite. Atmos. Chem. Phys. **6**, 925–946 (2006).
61. Kuang, Y. *et al.* Distinct diurnal variation in organic aerosol hygroscopicity and its relationship with oxygenated organic aerosol. Atmos. Chem. Phys. **20**, 865–880 (2020).
62. Sun, Y. *et al.* Chemical differences between PM1 and $PM_{2.5}$ in highly polluted environment and implications in air pollution studies. Geophys. Res. Lett. **47**, e2019GL086288 (2020).
63. Boylan, J. W. & Russell, A. G. PM and light extinction model performance metrics, goals, and criteria for three-dimensional air quality models. Atmos. Environ. **40**, 4946–4959 (2006).

Figures

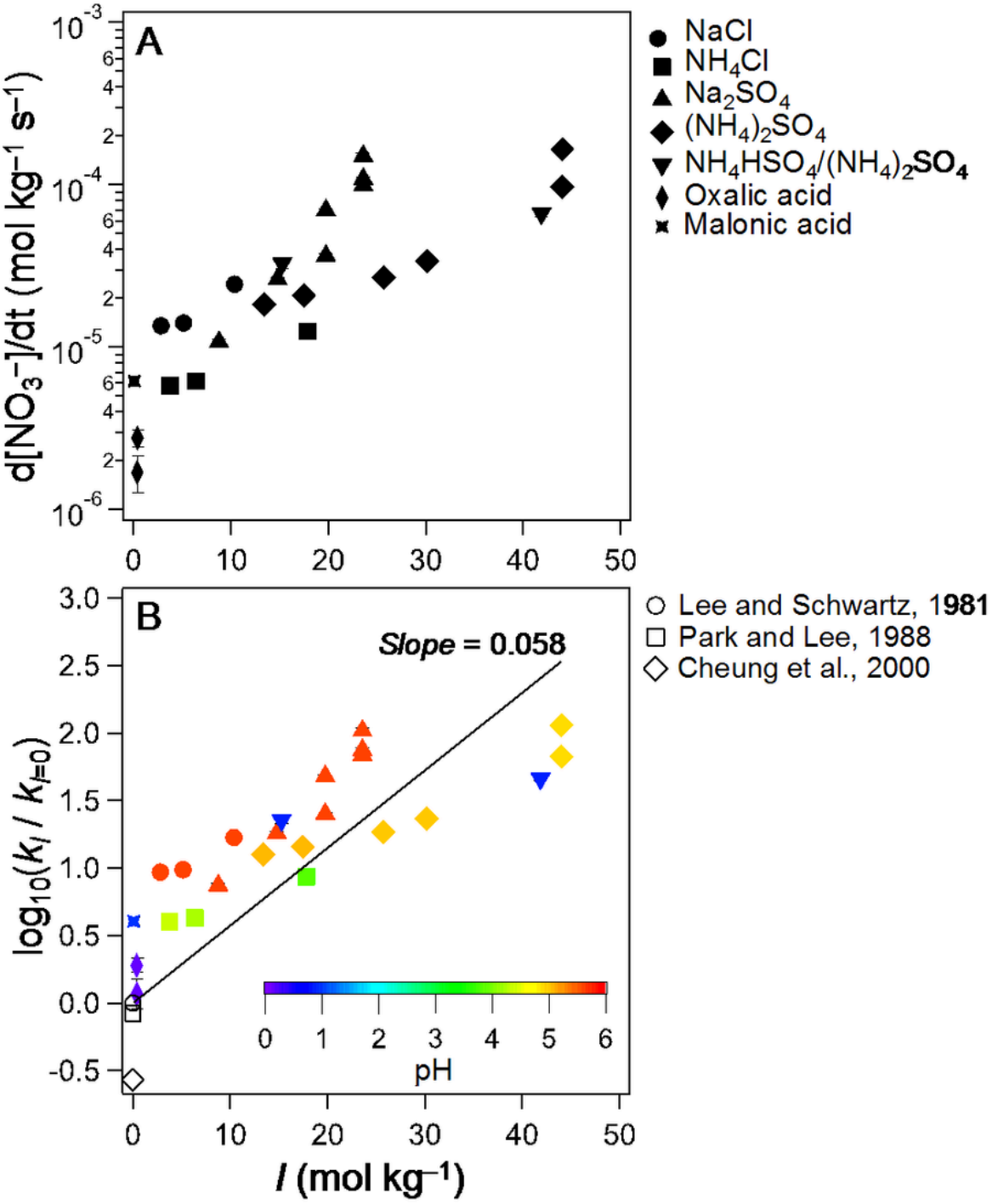

Figure 1

(A) Nitrate formation rates, $d[NO_3^-]/dt$, as a function of ionic strength, I, for all particle types. (B) The base-10 logarithm of observed reaction rate constants of R1 at a given I, k_I, normalized by that at infinite dilution, $k_{I=0}$, with color representing the initial pH of the particle. $k_{I=0}$ was assumed to be 1.0×10^8 mol^{-1} kg s^{-1} [3]. The empty symbols indicate the reported rate constants of R1 under diluted conditions [3–5]. The

solid line is a linear fit to all the data. The slope and the coefficient of determination of the solid line are 0.058 and 0.83, respectively. Error bars represent one standard deviation from triplicate Raman measurements. A molar ratio of ammonium bisulfate to ammonium sulfate (▼) was 0.5.

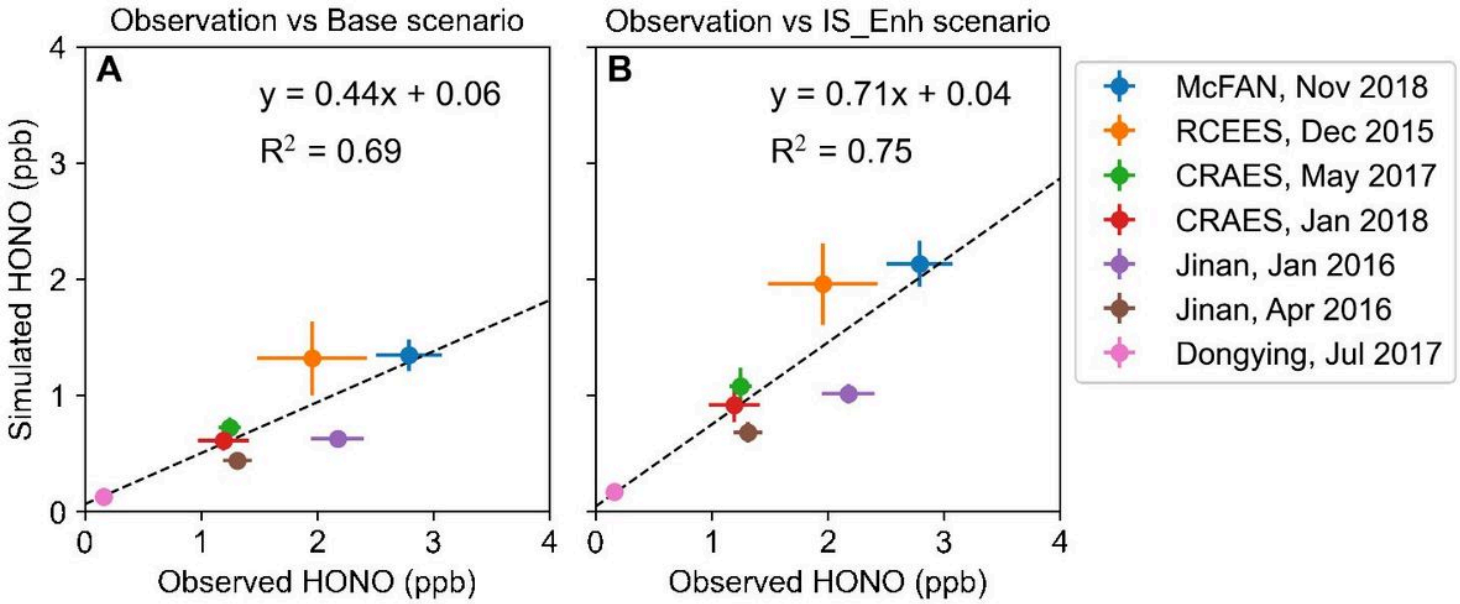

Figure 2

Linear regressions of the modeled and observed HONO concentrations at the North China Plain. Model results from the base and IS_Enh scenarios are shown in (**A**) and (**B**), respectively. The dots and error bars indicate the daily means and the standard errors of the means.

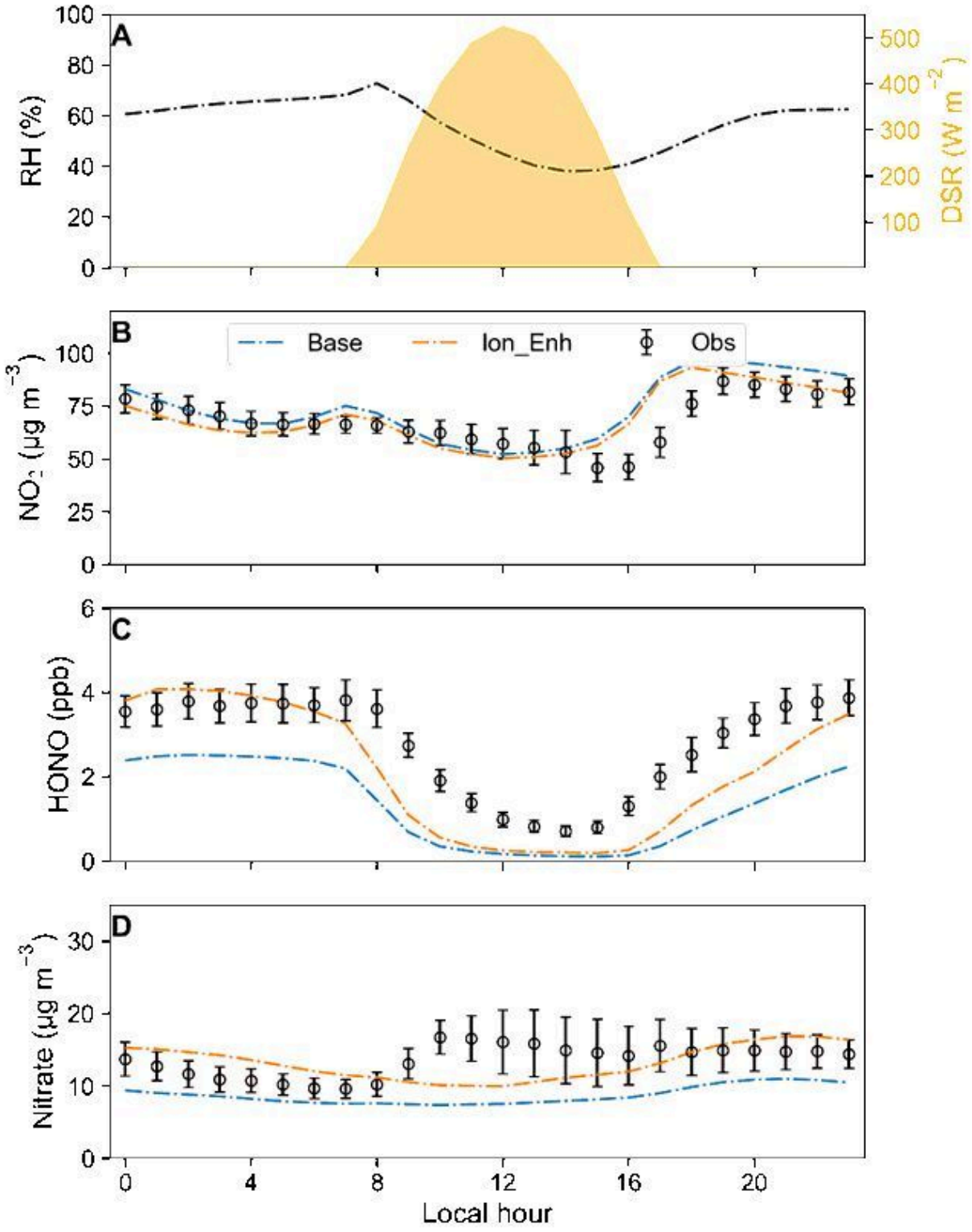

Figure 3

Model–observation comparison during the McFAN field campaign in winter 2018. Diurnal patterns of meteorological parameters (relative humidity (RH) and downward shortwave radiation (DSR)) (**A**), NO_2 (**B**), HONO (**C**), and particulate nitrate (**D**). The hourly means and the standard errors of the means from the observations and the mean values from two model scenarios, Base and IS_Enh, are shown. The shaded areas in (**B**), (**C**), and (**D**) indicate the differences between the two scenarios.

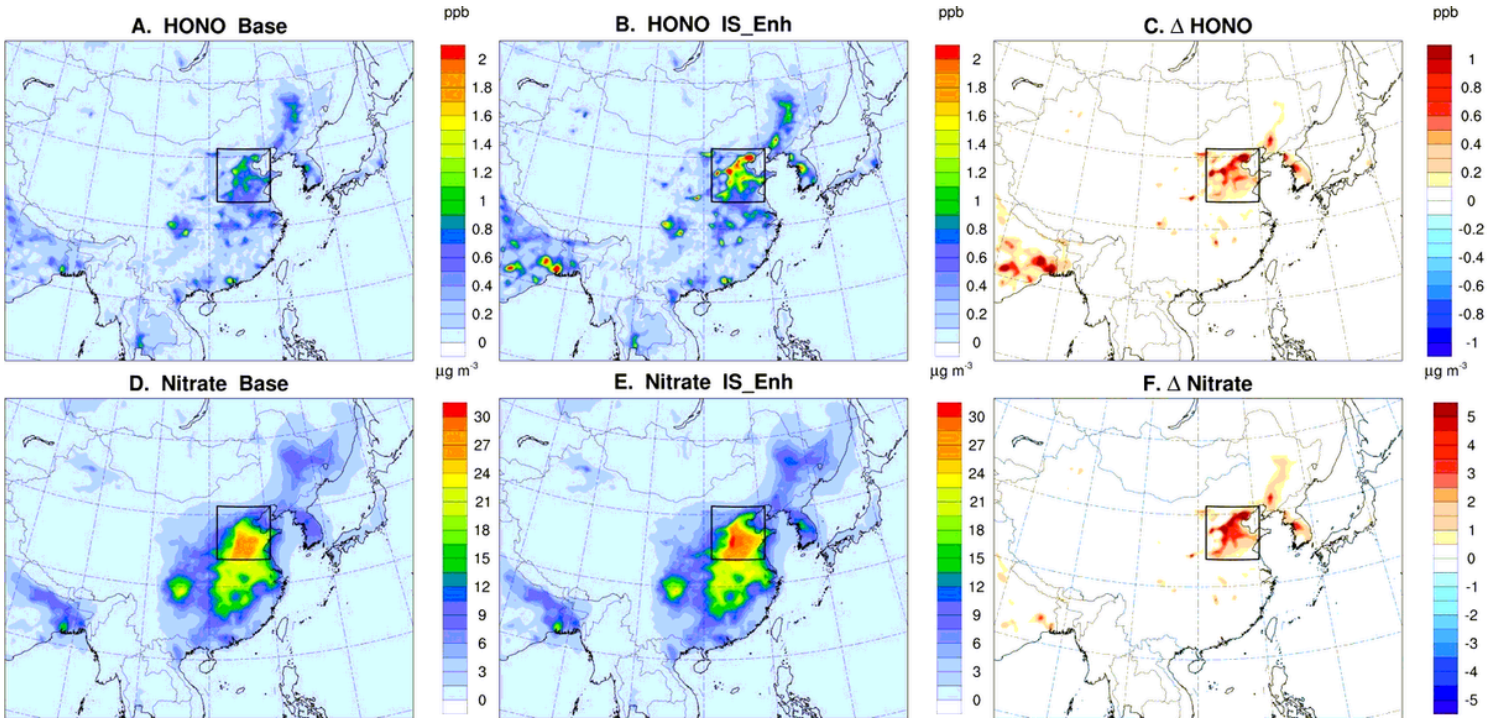

Figure 4

Spatial distribution of surface HONO and nitrate concentrations over East Asia during winter 2018. Model results are shown for the Base (**A** and **D**) and IS_Enh (**B** and **E**) scenarios and their differences (Δ = IS_Enh − Base) (**C** and **F**). The squares mark the North China Plain.

Supplementary Files

This is a list of supplementary files associated with this preprint. Click to download.

- GenetalNO2SI20221124.pdf